J Adv Ceram

Research Article

Enhanced in-plane ferroelectric polarizations with low in-plane leakage currents in Ca-doped $SrBi_2Ta_2O_9$ textured ceramics

Huijiadai Luo[1,2], Fangzhe Li[1,2], Jingxin Tian[1,2], Weiwei Zhang[1], Hua Ke[1,2]✉

Cite this article: Luo H, Li F, Tian J, et al. *J Adv Ceram* 2026, **15**(8): 9221344. https://doi.org/10.26599/JAC.2026.9221344

ABSTRACT: The Aurivillius-phase layered material $SrBi_2Ta_2O_9$ possesses an extremely low leakage current (~10^{-9} A·cm^{-2}) along the out-of-plane direction with in-plane ferroelectricity, which brings difficulties in achieving high ferroelectric performance and low leakage current simultaneously in randomly oriented ceramics. Here, highly textured $SrBi_2Ta_2O_9$ ceramics with a texture degree of $f = 0.985$ are prepared using templated grain growth (TGG) technology with a tape-casting method. The in-plane remnant polarization achieves 15.83 μC·cm^{-2}, which is increased by 197% compared with that of the $SrBi_2Ta_2O_9$ randomly oriented ceramic. Doping Ca is found to reduce the in-plane leakage current density to $J = 5.924\times10^{-7}$ A·cm^{-2}, which is attributed to the increased electronic band gap. This research presents an effective route for developing high-performance $SrBi_2Ta_2O_9$-based ferroelectric devices.

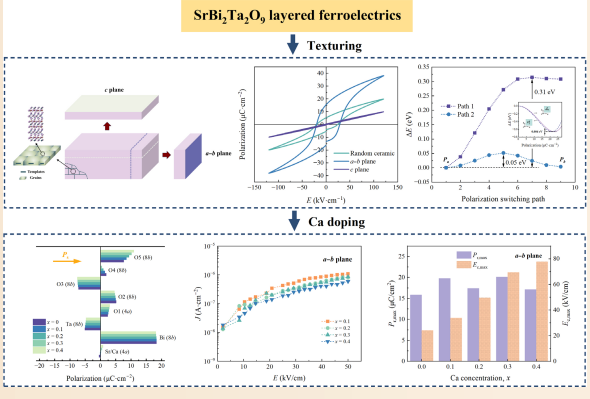

KEYWORDS: textured $SrBi_2Ta_2O_9$ ceramics; ferroelectric remnant polarization; Ca doping; in-plane leakage current; first-principles calculations

1 Introduction

The Aurivillius-phase layered material $SrBi_2Ta_2O_9$ is a lead-free ferroelectric material with extremely low leakage current characteristics (~10^{-9} A·cm^{-2}) [1], holding great potential for applications in semiconductor integrated circuits such as nonvolatile ferroelectric memories, dielectric microwave devices, and high-sensitivity sensors [2,3]. Compared with perovskite-type ferroelectric materials such as $BaTiO_3$ and $Pb(Zr,Ti)O_3$ (PZT) [4], however, the remnant polarization (P_r) of $SrBi_2Ta_2O_9$ randomly oriented ceramic is relatively low (~7 μC·cm^{-2}) [5], which inhibits the ferroelectric performance in the demand for low leakage current.

This contradiction comes from the structural anisotropy of layered $SrBi_2Ta_2O_9$. The orientation of the softening ferroelectric phonon mode is along the *a*-axis of the $SrBi_2Ta_2O_9$ lattice, while the orientation of alternately arranged $(Bi_2O_2)^{2+}$ layers, avoiding the migration of space charges, is along the *c*-axis. For actual $SrBi_2Ta_2O_9$ materials, when grains are randomly oriented, although the overall leakage current could be very low, the switching of ferroelectric domains under an external electric field is further constrained by the grain boundaries between differently oriented neighboring grains [6], which results in low P_r. Textured engineering via templated grain growth (TGG) technology can prepare polycrystalline ceramics with highly oriented grains [7–16], which can be applied to $SrBi_2Ta_2O_9$ to improve P_r. However, $SrBi_2Ta_2O_9$ textured ceramics have not achieved a high degree of orientation to fully release the in-plane ferroelectric performance (a Lotgering factor $f \approx 0.4$ is obtained) because the template grains are not uniformly aligned via conventional uniaxial pressing [17,18]. To improve the degree of orientation, a tape-casting processing method that has been used to prepare other Aurivillius-phase textured ceramics [14–16] is expected to be applied for $SrBi_2Ta_2O_9$. In addition, texture engineering cannot directly solve the problem of leakage current in the *a*–*b* plane. Introducing doping elements has been found to reduce the overall leakage current in $SrBi_2Ta_2O_9$ thin films and ceramics [19,20]. In particular, substitution of A-site Sr ions by Ca ions can simultaneously improve the Curie temperature (T_C) and P_r of $SrBi_2Ta_2O_9$ [19,21–24]. However, the mechanism of controlling ferroelectricity and leakage current behavior by Ca doping has not been understood in $SrBi_2Ta_2O_9$ materials, and how Ca doping influences the microstructure of $SrBi_2Ta_2O_9$ textured ceramics has not been studied.

In this work, highly textured $SrBi_2Ta_2O_9$ ceramics with $f = 0.985$ are successfully fabricated via the TGG method and a tape-casting

[1] School of Materials Science and Engineering, Harbin Institute of Technology, Harbin 150001, China. [2] State Key Laboratory of Precision Welding & Joining of Materials and Structures, School of Materials Science and Engineering, Harbin Institute of Technology, Harbin 150001, China.

✉ Corresponding author. E-mail: hua_ke@hit.edu.cn

Received: May 5, 2026; Revised: June 21, 2026; Accepted: July 3, 2026

processing method, fully releasing the ferroelectric properties in the *a*–*b* plane with P_r = 15.83 μC·cm^{-2}, which is an increase of 197% compared with randomly oriented ceramics. By Ca doping while maintaining a high degree of orientation ($f \geq 0.917$), the Curie temperature is enhanced from 298 to 500 °C, and the room-temperature leakage current density in the *a*–*b* plane is reduced to 5.924×10^{-7} A·cm^{-2} (@50 kV·cm^{-1}). According to first-principles calculations, the reduction in the in-plane leakage current derives from the increased electronic band gap by Ca substitution. Overcoming the limitation of randomly oriented grains and the in-plane leakage current, the comprehensive ferroelectric performance of $SrBi_2Ta_2O_9$ ceramics is enhanced, providing a new technical route for the design of $SrBi_2Ta_2O_9$ ferroelectric devices.

2 Experimental

2.1 Preparation of $SrBi_2Ta_2O_9$ and Ca-doped $SrBi_2Ta_2O_9$ textured ceramics

The molten salt synthesis method was used to synthesize $SrBi_2Ta_2O_9$ template powders. The metal oxides of Bi_2O_3 (99.5%, Aladdin) and Ta_2O_5 (99.5%, Aladdin) and the metal carbonate $SrCO_3$ (99.5%, Aladdin) were weighed for the compound $SrBi_2Ta_2O_9$, and a 1 : 1 equimolar mixture of NaCl (99.9%, Aladdin) and KCl (99.9%, Aladdin) was then added. The above raw powders were ball-milled for 12 h with zirconia media in ethanol. After drying, the powders were calcined at 1100 °C for 1 h. The final powders were repeatedly cleaned with deionized water. During this process, the content of Cl^- ions was tested by an $AgNO_3$ solution to eliminate the residual salts.

The solid-state reaction method was used to synthesize $SrBi_2Ta_2O_9$ and $Sr_{1-x}Ca_xBi_2Ta_2O_9$ (x = 0.1, 0.2, 0.3, and 0.4) matrix powders. Stoichiometric quantities of Bi_2O_3 (99.5%, Aladdin), Ta_2O_5 (99.5%, Aladdin), $SrCO_3$ (99.5%, Aladdin), and $CaCO_3$ (99.0%, Aladdin) raw powders were mixed with ZrO_2 balls and ethyl alcohol and then ball-milled for 24 h. The dried raw material powders were calcined at 750 °C for 2 h. To further reduce the particle size of the matrix powders, the pre-calcined powders were ball-milled again for 24 h.

$SrBi_2Ta_2O_9$ and $Sr_{1-x}Ca_xBi_2Ta_2O_9$ textured ceramics were prepared through a tape-casting method and a conventional pressureless sintering process. To efficiently prepare ceramics with all the compositions, pure $SrBi_2Ta_2O_9$ templates of 5 vol% were used for both $SrBi_2Ta_2O_9$ and $Sr_{1-x}Ca_xBi_2Ta_2O_9$ textured ceramics. First, $SrBi_2Ta_2O_9$ templates, $SrBi_2Ta_2O_9$ (or $Sr_{1-x}Ca_xBi_2Ta_2O_9$) matrix powders, solvents, binders, dispersants, and plasticizers were mixed into slurries for 48 h to avoid aggregations of template and matrix powders. The volume ratio of powders and additives is approximately 1 : 5. After vacuum degassing, the slurry was tape-cast with a blade gap of 200 μm and a casting rate of 6 mm·s^{-1}, then dried at room temperature, and cut into green tapes with a size of 10 mm × 10 mm. Laminating 20–30 green tapes at 60 MPa, $SrBi_2Ta_2O_9$ and $Sr_{1-x}Ca_xBi_2Ta_2O_9$ green bodies were obtained and then compacted by cold isostatic pressing at 200 MPa. After a thermal treatment at 600 °C for 1 h to remove organic residues, the green bodies were sintered at 1125 °C for 3 h in an O_2 atmosphere to obtain $SrBi_2Ta_2O_9$- and $Sr_{1-x}Ca_xBi_2Ta_2O_9$-textured ceramics. For comparison, a traditional solid-state reaction method was adopted to obtain the randomly oriented $SrBi_2Ta_2O_9$ ceramics, which were also sintered at 1125 °C for 3 h in an O_2 atmosphere.

2.2 Characterization

The phase structure and degree of texture were examined by an X-ray diffractometer (XRD; X'Pert Pro, PANalytical, the Netherlands) with a Cu Kα radiation source (λ = 1.540598 Å, 40 kV, and 40 mA). Grain morphologies and nanoscale structures of textured ceramics were characterized through a scanning electron microscope (SEM; Merlin Compact, ZEISS, Germany and Amber, TESCAN, Czech Republic) and a transmission electron microscope (TEM; Thermo Scientific Talos F200X G2, Waltham, USA), respectively. A scanning electron microscope (SEM; Hitachi SU5000, Hitachi, Japan) equipped with an electron backscatter diffraction (EBSD) detector (Symmetry C-Nano$^+$, Oxford, UK) was used to obtain elemental distribution and orientation information. Room-temperature dielectric properties were measured by a precision impedance analyzer (Agilent 4294A, Keysight Technologies Inc., USA). Temperature-dependent dielectric properties and alternating current (AC) impedance were measured by an LCR meter TH2827C (Tonghui Electronic Co., Ltd., China). The direct current (DC) conductivity of the sample was obtained by fitting the DC resistance of the AC impedance spectrum using $\sigma_{dc} = t/(RS)$, where σ_{dc} is the DC conductivity; t is the thickness of the sample; R is the fitted DC resistance; S is the area of the sample. Room-temperature ferroelectric properties (*P*–*E* hysteresis loops) and current–voltage (*I*–*V*) curves were measured via a ferroelectric tester (Precision Premier II, Radiant Technologies Inc., USA). Leakage current behaviors were analyzed by *I*–*V* curves, which were tested using an unswitched triangular mode; an absolute preset field of 50 kV·cm^{-1} for 100 ms was first applied, and then a stepwise pulse field was used to test the current until it reached a maximum field of 50 kV·cm^{-1}.

2.3 Computational methods

First-principles calculations were performed using the QUANTUM ESPRESSO code [25–27] within the generalized gradient approximation (GGA) [28] with the Perdew–Burke–Ernzerhof parametrization revised for solids (PBEsol) [29]. Ultrasoft pseudopotentials [30] were adopted to generate valence states of $4s^24p^65s^2$ for Sr, $3s^23p^64s^2$ for Ca, $5d^{10}6s^26p^3$ for Bi, $5s^25p^65d^36s^2$ for Ta, and $2s^22p^4$ for O. A ferroelectric ground-state structure of $SrBi_2Ta_2O_9$ with an orthorhombic phase ($A2_1am$ space group) was constructed. The experimental lattice parameters a = 5.531 Å, b = 5.534 Å, and c = 24.98 Å (conventional unit cell with 56 atoms) [31] were used as initial values for structural optimization. To accelerate computations, the $SrBi_2Ta_2O_9$ primitive cell containing 28 atoms was used, setting a plane-wave energy cutoff of 50 Ry and a 2 × 2 × 4 Monkhorst–Pack self-consistency mesh. To efficiently mimic the experimental compositions, the virtual crystal approximation (VCA) method [32,33] was further applied to construct $Sr_{1-x}Ca_xBi_2Ta_2O_9$ (x = 0.1, 0.2, 0.3, and 0.4) unit cells by mixing pseudopotentials of Sr and Ca. Polarization switching paths and the migration paths of oxygen vacancies were determined by the climbing image nudged elastic band (CI-NEB) method [34,35]. The polarization values of each intermediate state on the switching path were calculated by $P = \Sigma_i(m_i \times \Delta x_i \times Q_i e)/V$, where m_i is the site multiplicity; Δx_i is the atomic displacement of the i-th ion along the a-axis from the corresponding position of the paraelectric tetragonal structure; $Q_i e$ is the ionic charge of the i-th ion; V is the unit-cell volume.

3 Results and discussion

Figure 1 shows the phase structures and the morphologies of the $SrBi_2Ta_2O_9$ textured ceramic with a comparison of randomly oriented ceramics. The two samples marked by the *c* plane and *a*–*b* plane in Fig. 1(a) denote that the normal direction of the

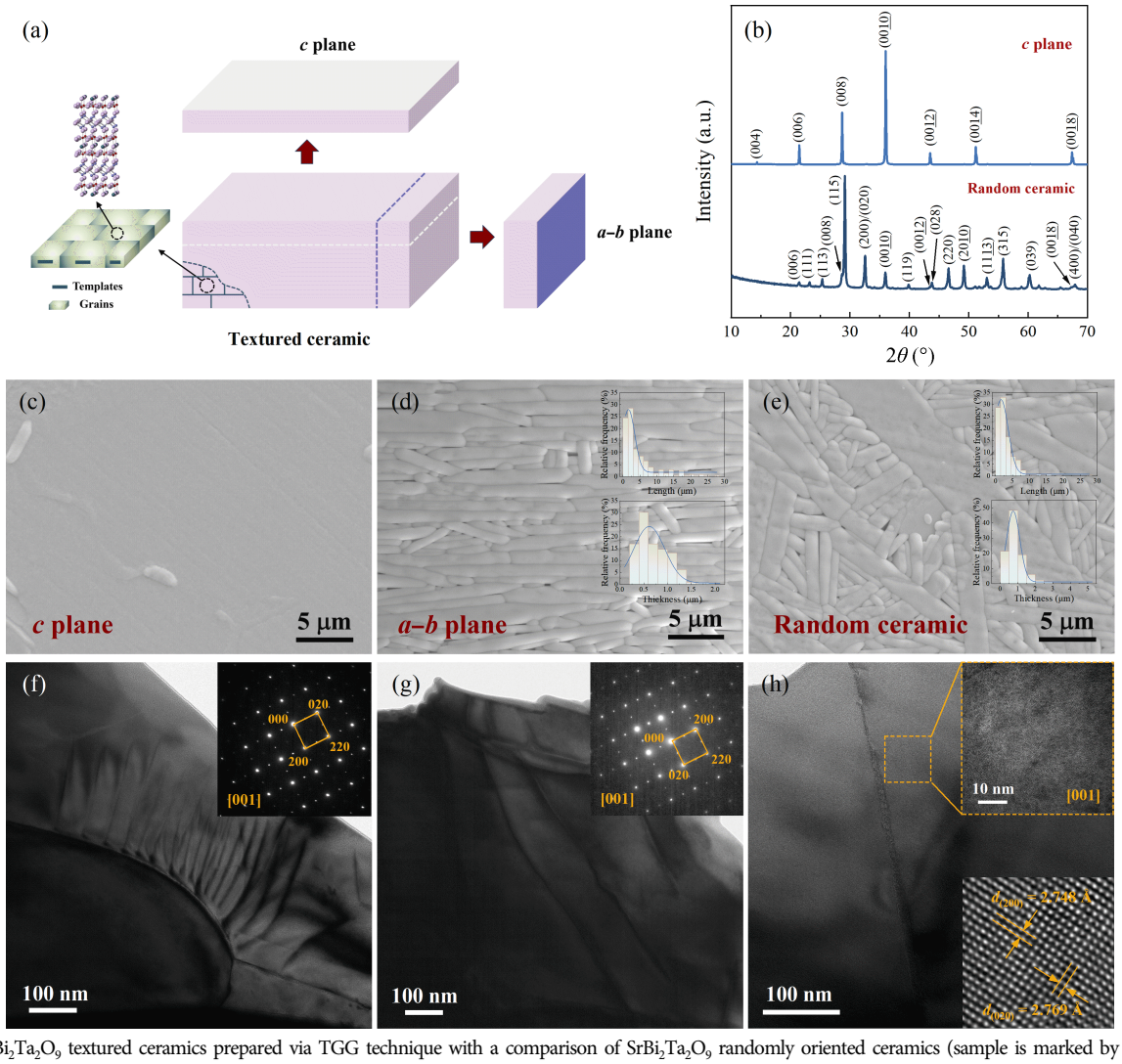

Fig. 1 $SrBi_2Ta_2O_9$ textured ceramics prepared via TGG technique with a comparison of $SrBi_2Ta_2O_9$ randomly oriented ceramics (sample is marked by a random ceramic sample). (a) Schematic diagrams of $SrBi_2Ta_2O_9$ textured ceramics with two samples marked by *c* plane and *a*–*b* plane. (b) XRD patterns of *c* plane and random ceramic samples sintered at 1125 °C. SEM secondary electron images of (c) *c* plane sample, (d) *a*–*b* plane sample, and (e) random ceramic sample. Insets are length and thickness distributions of grains analyzed by ImageJ software. (f, g) TEM bright-field images with SAED patterns and (h) high-resolution TEM (HRTEM) images of three different grains of *c* plane sample.

sample surface is perpendicular to and coplanar with the ferroelectric polarization direction, respectively. In Fig. 1(b), the XRD pattern of the random ceramic sample corresponds to orthorhombic $A2_1am$ symmetry, and the *c* plane sample exhibits pure (00*l*) Bragg diffraction peaks. By calculating the Lotgering factor $f = (P - P_0)/(1 - P_0)$ [36–38] from the intensities (I) of diffraction peaks, where P and P_0 denote $\Sigma I_{(00l)}/\Sigma I_{(hkl)}$ in textured and randomly oriented ceramics, respectively, the obtained degree of texture is $f = 0.985$, which shows strong preferential orientation close to the $SrBi_2Ta_2O_9$ single crystal [39]. The morphologies of the *c* plane and *a*–*b* plane samples in Figs. 1(c) and 1(d) confirm the anisotropic grain growth during the sintering process of $SrBi_2Ta_2O_9$ textured ceramics in comparison with the random ceramic sample (Fig. 1(e)). In Figs. 1(f) and 1(g), the TEM images of the *c* plane sample further verify the most *c*-axis orientation of $SrBi_2Ta_2O_9$ grains with random orientations of the *a*- and *b*-axes, and the in-plane distribution of 90° domains is also confirmed by the appearance of (100) and (010) superlattice spots in selected area electron diffraction (SAED) patterns.

For dielectric properties at room temperature (Fig. 2(a)), the permittivity (ε_r) and dielectric loss (tanδ) of the *a*–*b* plane sample are almost independent of the frequency from 5 kHz to 2 MHz, exhibiting strong stability of the dielectric performance of $SrBi_2Ta_2O_9$. With the temperature increasing at a frequency of 1 MHz (Fig. 2(b)), the maximum ε_r and the phase transition Curie temperature T_C of the *a*–*b* plane sample are 776.7 and 298 °C, respectively, the former of which is larger than that of the previous $SrBi_2Ta_2O_9$ textured ceramic (~580 °C) [17] and the latter of which is in agreement with previously reported values (~300 °C) [5,17,40]. In Fig. 2(c), the ferroelectric properties exhibit anisotropy between the *c* plane and *a*–*b* plane samples. The remnant polarization P_r of the *a*–*b* plane sample reaches 15.83 μC·cm^{-2}, which is increased by 197% compared with that of the randomly oriented ceramic (5.33 μC·cm^{-2}). Table 1 compares the P_r and coercive field (E_c) among several $SrBi_2Ta_2O_9$ textured ceramics, randomly oriented ceramics, and single crystals [17,41–44], indicating excellent ferroelectric properties of the obtained $SrBi_2Ta_2O_9$ textured ceramic.

In Fig. 2(d), the large P_r of the *a*–*b* plane sample of $SrBi_2Ta_2O_9$ textured ceramics could be attributed to the easy polarization switching from the *a*-axis (P_a) to the *b*-axis (P_b). To avoid breaking the lattice symmetry that conforms to the actual switching process, two hypothetical switching paths from P_a to P_b are constructed and exhibit energy barriers of 0.31 and 0.05 eV,

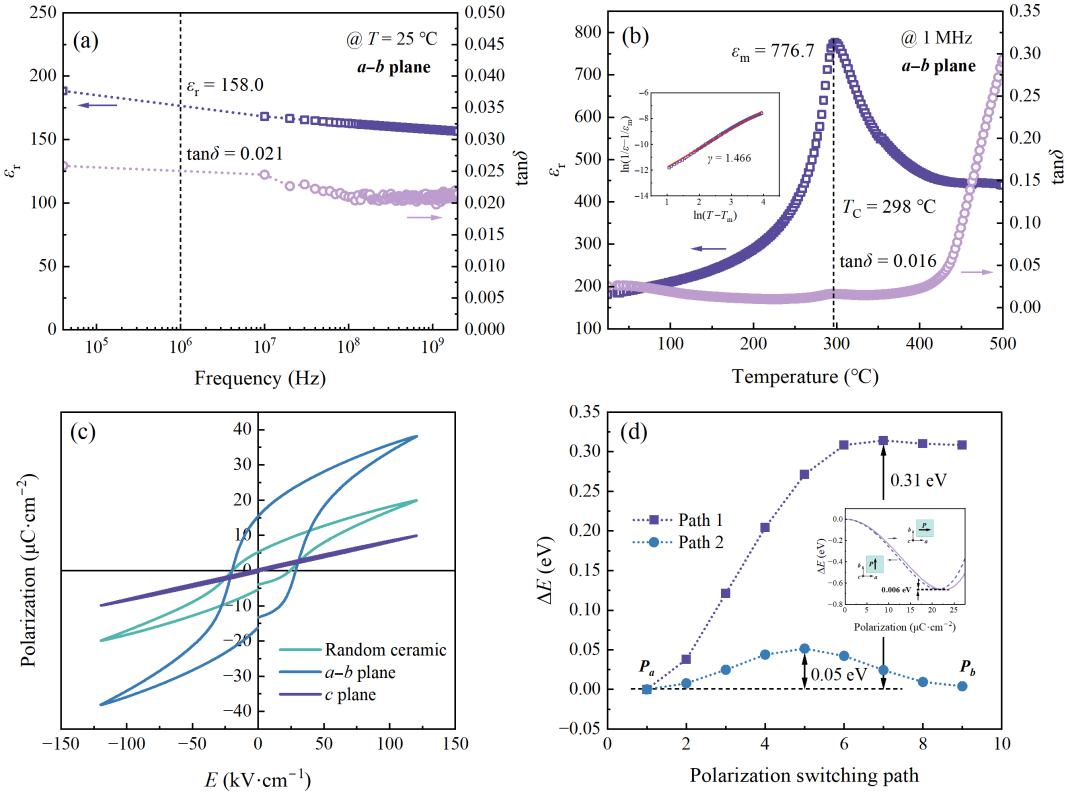

Fig. 2 Electrical properties of $SrBi_2Ta_2O_9$ textured ceramics. (a) Frequency-dependent ε_r and tanδ of *a*–*b* plane sample at room temperature. (b) Temperature-dependent ε_r and tanδ of *a*–*b* plane sample at a frequency of 1 MHz. (c) *P*–*E* hysteresis loops of *c* plane, *a*–*b* plane, and random ceramic samples. (d) Polarization switching path from *a*- to *b*-axis calculated by CI-NEB method (path 1: change in oxygen octahedral tilting is not included from *a*- to *b*-axis; path 2: atomic displacements of oxygen octahedral tilting for both *a*- and *b*-axes are ignored). Inset of panel (d) shows total energy differences varying with polarization for standard $SrBi_2Ta_2O_9$ unit cell and $SrBi_2Ta_2O_9$ unit cell in which polarization is along *b*-axis (total energy of paraelectric state is chosen as reference energy), fitted by polarization switching paths obtained by first-principles calculations and CI-NEB method.

Table 1 Comparison of ferroelectric performance in $SrBi_2Ta_2O_9$ textured ceramics (*a*–*b* plane), random ceramics, and single crystals.

Material form	P_r (μC·cm^{-2})	E_c (kV·cm^{-1})	E_{max} (kV·cm^{-1})	Ref.
$SrBi_2Ta_2O_9$ textured ceramic (*a*–*b* plane)	15.83	24.18	120	This work
$SrBi_2Ta_2O_9$ random ceramic	5.33	22.04	120	This work
$SrBi_2Ta_2O_9$ textured ceramic (*a*–*b* plane)	~6	~25	150	[17]
$SrBi_2Ta_2O_9$ textured ceramic (*a*–*b* plane)	4.8	~25	110	[42]
$SrBi_2Ta_2O_9$ random ceramic	~5.6	~20	60	[43]
$SrBi_2Ta_2O_9$ single crystal (*a*–*b* plane)	14	22	62.5	[41]
$SrBi_2Ta_2O_9$ single crystal (*a*–*b* plane)	12	39.7	61	[44]

Note: E_{max} is applied external electric field of *P*–*E* hysteresis loops (P_s will be listed for $SrBi_2Ta_2O_9$ single crystal if P_r is not provided in literature).

respectively. In addition, the large P_r of the *a*–*b* plane sample can also be understood by the small energy difference of ferroelectric polarizations between the *a*- and *b*-axis lattice orientations, as shown in the inset of Fig. 2(d). The total energy differences (ΔE) varying with polarization show that the energy difference at the theoretical spontaneous polarization (P_s) between the *a*- and *b*-axes is 0.006 eV. Such a small energy difference indicates that polarization can exist along the *a*- and *b*-axes during the synthesis of $SrBi_2Ta_2O_9$ textured ceramics. Even though the grain directions of the *a*- and *b*-axes are randomly distributed in the *a*–*b* plane of $SrBi_2Ta_2O_9$ textured ceramics, the polarization directions could be highly aligned, contributing to a large P_r in any specific direction of the *a*–*b* plane. The mechanism is slightly different from our previously reported one in $BaTiO_3$-based textured ceramics [45].

Figures 3(a)–3(c) illustrate the effect of doped Ca on the structural and ferroelectric properties in $SrBi_2Ta_2O_9$ via first-principles calculations. As schematically shown in Fig. 3(a), O1, O2, O4, and O5 atoms belong to the TaO_6 octahedron in which O1 lies in the Sr–O plane and the position of O2 is opposite to O1 along the *c*-axis. O4 and O5 lie in the Ta–O plane, which shares the same equivalent positions in the high-symmetry tetragonal phase (space group *I*4/*mmm*). In Fig. 3(b), both P_s and the total energy difference between the paraelectric and ferroelectric states increase with increasing *x*, exhibiting enhanced ferroelectric polarization and stability. Extracting the atomic contributions of P_s (Fig. 3(c)) reveals that Ca doping contributes to the enhanced polarization of the $[(Sr/Ca)Ta_2O_7]^{2-}$ perovskite unit by increasing the bond length difference between the Ta–O5 and Ta–O4 bonds. Figures 3(d)–3(g) show the phase structures and morphologies of textured $Sr_{1-x}Ca_xBi_2Ta_2O_9$ (x = 0.1, 0.2, 0.3, and 0.4) ceramics. With Ca doping, the degree of texture decreases from f = 0.959 at x = 0.1 to f = 0.917 at x = 0.4 with the appearance of a small

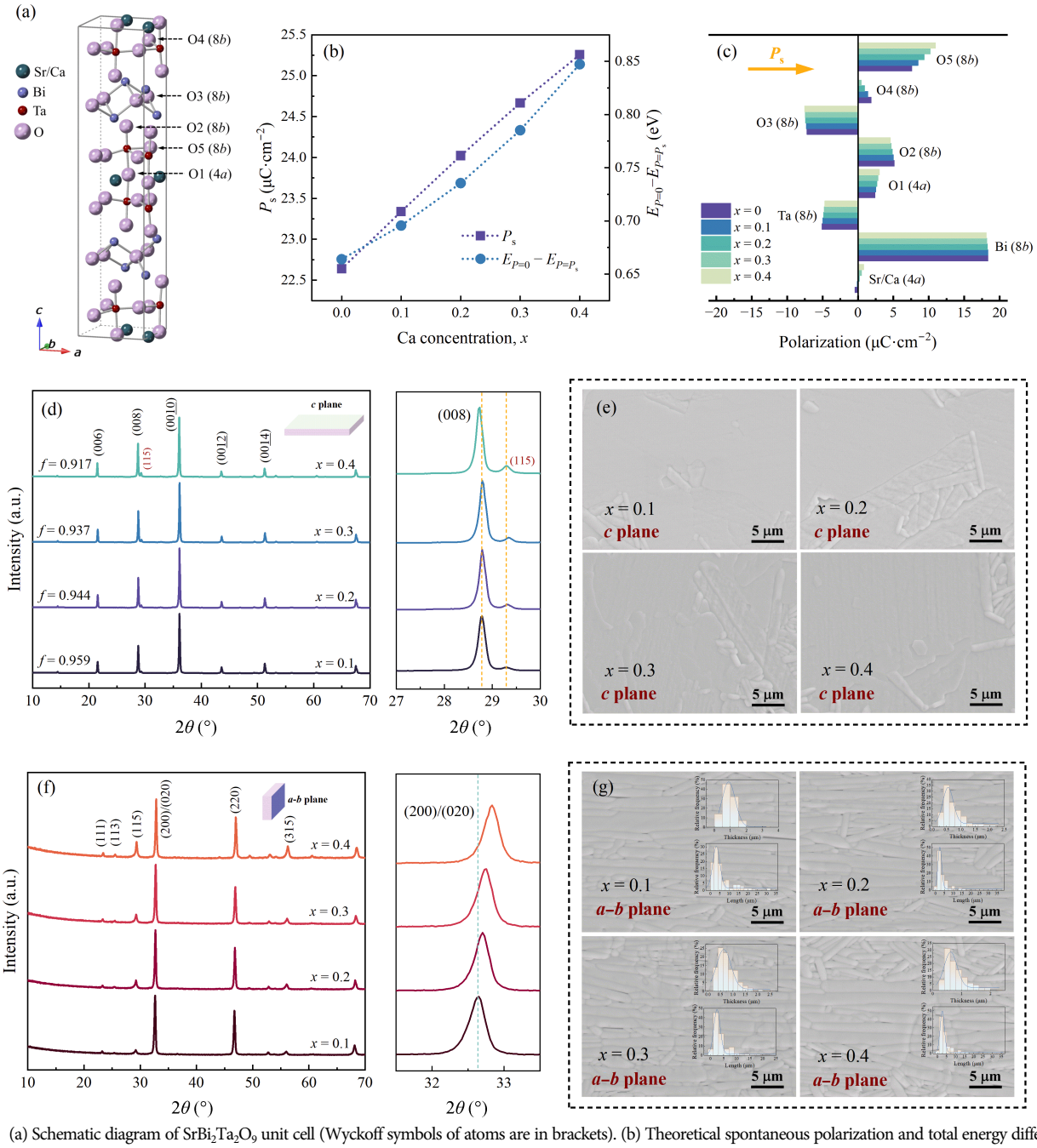

Fig. 3 (a) Schematic diagram of $SrBi_2Ta_2O_9$ unit cell (Wyckoff symbols of atoms are in brackets). (b) Theoretical spontaneous polarization and total energy difference between paraelectric and ferroelectric states of $Sr_{1-x}Ca_xBi_2Ta_2O_9$ unit cells. (c) Atomic contributions of theoretical spontaneous polarization of $Sr_{1-x}Ca_xBi_2Ta_2O_9$ unit cells (for atomic displacements, paraelectric structure is chosen as reference such that unweighted average of displacements vanishes). XRD patterns and SEM images of (d, e) *c* plane samples and (f, g) *a*–*b* plane samples of textured $Sr_{1-x}Ca_xBi_2Ta_2O_9$ ceramics. Insets of panel (g) are length and thickness distributions of grains.

diffraction peak from the (115) plane. According to the refined lattice parameters (Fig. S5 in the Electronic Supplementary Material (ESM)), the doped Ca^{2+} ions lead to shrinkages of the lattice by −0.67%, −0.62%, and −0.18% for the *a*-, *b*-, and *c*-axes, respectively. Such lattice mismatch between $SrBi_2Ta_2O_9$ template grains and $Sr_{1-x}Ca_xBi_2Ta_2O_9$ matrix grains gives rise to the reduced texture degree in the heteroepitaxial TGG process [7]. In Figs. 3(e) and 3(g), the grain morphologies characterized by SEM also exhibit a small amount of randomly oriented grains with increasing Ca content. The EBSD images of the *c* plane samples for $x = 0$ and 0.4 verify the large amount of [00*l*]-oriented grains (Fig. S6 in the ESM), verifying the high degree of texture in the $Sr_{1-x}Ca_xBi_2Ta_2O_9$ ceramics.

Figure 4 investigates the in-plane electrical properties and leakage current behaviors of textured $Sr_{1-x}Ca_xBi_2Ta_2O_9$ ceramics. In Figs. 4(a) and 4(b), the frequency-dependent ε_r and tanδ at room temperature decrease with increasing x for the *a*–*b* plane samples of textured $Sr_{1-x}Ca_xBi_2Ta_2O_9$ ceramics. In particular, the tanδ of the *a*–*b* plane sample decreases from 0.021 for pure textured $SrBi_2Ta_2O_9$ ceramics to 0.006 for the $x = 0.4$ composition, one order of magnitude lower than 0.04–0.08 for $Sr_{1-x}Ca_xBi_2Ta_2O_9$ thin films, and the trend with Ca concentration is opposite to that of thin films [19,23]. Such low dielectric loss of the *a*–*b* plane suggests low defect concentration and conductivity in textured $Sr_{1-x}Ca_xBi_2Ta_2O_9$ ceramics, which would exhibit good stability of high-frequency responses. In Fig. 4(c), the temperature-dependent ε_r for the *a*–*b* plane sample shows the enhancement of T_C from 300 °C for pure textured $SrBi_2Ta_2O_9$ ceramics to 500 °C for the $x =$

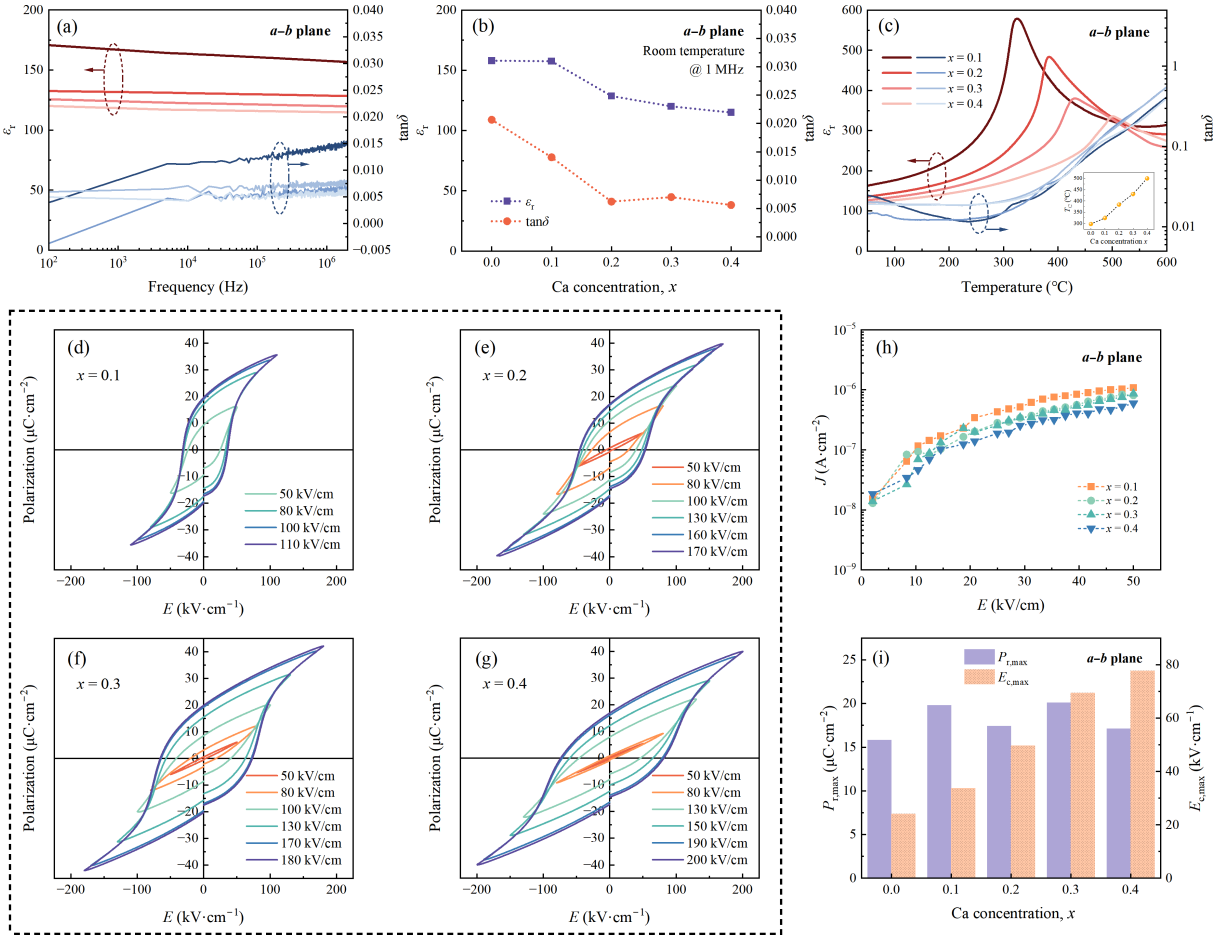

Fig. 4 Dielectric and ferroelectric properties of textured $Sr_{1-x}Ca_xBi_2Ta_2O_9$ ceramics (x = 0.1, 0.2, 0.3, and 0.4). (a) Frequency-dependent ε_r and tanδ of a–b plane samples at room temperature. (b) Comparisons of room-temperature ε_r and tanδ of a–b plane at a frequency of 1 MHz. (c) Temperature-dependent ε_r and tanδ of a–b plane samples in range of 50–600 °C (inset is change in T_C with Ca concentration). (d–g) P–E hysteresis loops of a–b plane samples. (h) Leakage current density (J) of a–b plane samples. (i) Comparisons of maximum P_r and E_c of a–b plane samples when reaching saturated hysteresis loops.

0.4 composition, which corresponds to previous observations [22,24,46] and is higher than ~470 and 400 °C for $Sr_{0.6}Ca_{0.4}Bi_2Ta_2O_9$ random ceramics and thin films, respectively [22,24]. Figures 4(d)–4(g) show ferroelectric P–E hysteresis loops of textured $Sr_{1-x}Ca_xBi_2Ta_2O_9$ ceramics. For a–b plane samples at x = 0.1–0.4, the maximum P_r when reaching saturated hysteresis loops is larger than that of pure textured $SrBi_2Ta_2O_9$ ceramics, confirming the enhancement of ferroelectric polarization with Ca doping [19,23,46]. Figure 4(h) shows the leakage current density (J) varying with the electric field of a–b plane samples. With x increasing, the leakage current density decreases to 5.924×10^{-7} A·cm^{-2} (@50 kV·cm^{-1}). This trend is opposite to that of $Sr_{1-x}Ca_xBi_2Ta_2O_9$ thin films, which derives from the increase in the conductivity of the film itself [19]. In Fig. 4(i), the overall maximum P_r is larger than that of pure textured $SrBi_2Ta_2O_9$ ceramics and verifies the result of first-principles calculations in Fig. 3(b). The oscillation of the polarization value may be attributed to the reduction in the texture degree.

To understand the intrinsic mechanism of the reduced in-plane leakage current by Ca doping, we conducted first-principles calculations of the electric band structure (Fig. 5(a)). The band gap extracted from electric band structures (Fig. S9 in the ESM) increases linearly with Ca doping, the trend of which coincides with the experimental band gaps of $SrBi_2Ta_2O_9$ and $CaBi_2Ta_2O_9$ measured by ultraviolet–visible (UV-vis) absorption edge [47] as well as calculated band gaps [48]. Thus, the possible electronic carrier mobility can be further inhibited by Ca doping. Figures 5(b) and 5(c) illustrate AC impedance measurements for a–b plane samples of textured $Sr_{1-x}Ca_xBi_2Ta_2O_9$ ceramics at various temperatures. In Fig. 5(b), the impedance spectra measured at 250 °C demonstrate the enhancement of the in-plane resistivity by Ca doping. Figure 5(c) shows the extracted Arrhenius plots of DC conductivities (σ_{dc}) in the temperature range of 350–600 °C. The σ_{dc} of the a–b plane sample decreases while the σ_{dc} of the c plane sample has a little change with Ca doping (Fig. S11 in the ESM). At T = 600 °C, σ_{dc} of the a–b plane sample decreases from 4.260×10^{-5} S·cm^{-1} at x = 0 to 2.927×10^{-5} S·cm^{-1} at x = 0.4. The fitted activation energy (E_a) of the a–b plane sample increases from 0.966 to 1.079 eV, which approaches the 1.090 eV of the c plane sample of pure textured $SrBi_2Ta_2O_9$ ceramic (Fig. S11 in the ESM). Both σ_{dc} and E_a prove that the in-plane leakage current at high temperatures above T_C is also weakened by Ca doping.

For actual high-temperature operating conditions, one could estimate the stable operating temperature based on Landau's theory of secondary phase transition, as given by Eq. (1):

$$G = G_0 + A_0 (T - T_C) P^2 + BP^4 \quad (1)$$

where G is the total free energy; G_0 is the free energy of the high-symmetry paraelectric phase; P is the ferroelectric polarization; T is the temperature; T_C is the Curie temperature; A_0 and B are constants. Setting $\partial G/\partial P$ = 0 yields Eqs. (2) and (3):

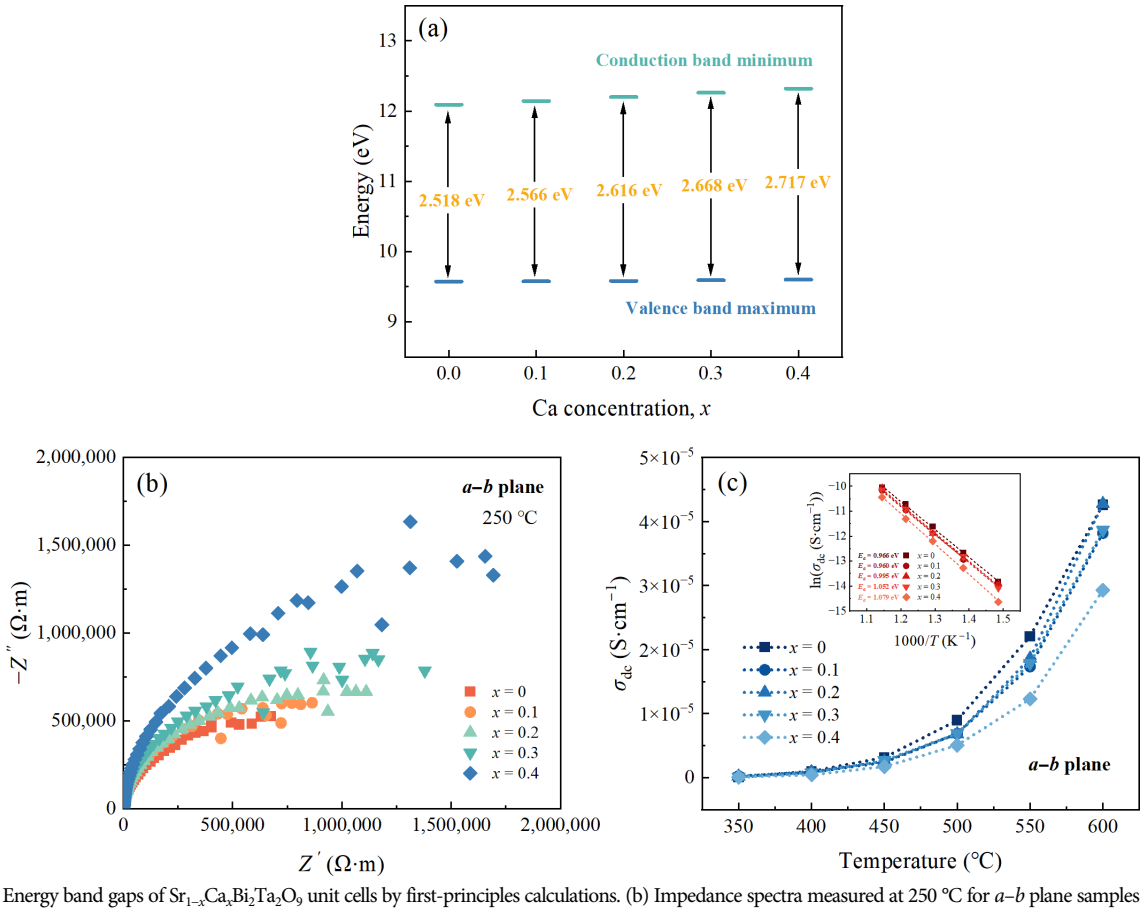

Fig. 5 (a) Energy band gaps of $Sr_{1-x}Ca_xBi_2Ta_2O_9$ unit cells by first-principles calculations. (b) Impedance spectra measured at 250 °C for *a*–*b* plane samples of textured $Sr_{1-x}Ca_xBi_2Ta_2O_9$ ceramics (x = 0, 0.1, 0.2, 0.3, and 0.4). (c) Arrhenius plots of DC conductivities for *a*–*b* plane samples of textured $Sr_{1-x}Ca_xBi_2Ta_2O_9$ ceramics, where inset shows activation energies extracted from Arrhenius plots of DC conductivities.

$$P = \sqrt{\frac{A_0}{2B}(T_C - T)} \tag{2}$$

$$\left(\frac{P}{P_s}\right)^2 = 1 - \frac{T}{T_C} \tag{3}$$

Considering the operating temperature $T = T_{opr}$ with the decline of the polarization by 50% (i.e., $P_{opt} = 0.5P_s$), which is regarded as a steady working condition, $T_{opr} = 0.75T_C$ is obtained. For x = 0–0.4, the estimated T_{opr} increases from 224 to 375 °C.

(i) Energy band gaps of $Sr_{1-x}Ca_xBi_2Ta_2O_9$ unit cells by first-principles calculations. (ii) Impedance spectra measured at 250 °C for *a*–*b* plane samples of textured $Sr_{1-x}Ca_xBi_2Ta_2O_9$ ceramics (x = 0, 0.1, 0.2, 0.3, and 0.4). (iii) Arrhenius plots of DC conductivities for *a*–*b* plane samples of textured $Sr_{1-x}Ca_xBi_2Ta_2O_9$ ceramics, where inset shows activation energies extracted from Arrhenius plots of DC conductivities.

In addition to the improved P_r of *a*–*b* plane samples of textured $SrBi_2Ta_2O_9$ ceramics in this work, the partially *a*-oriented $SrBi_2Ta_2O_9$ thin film has also been reported to exhibit a high P_r of 23.7 μC·cm^{-2} (E_c ≈ 140 kV·cm^{-1}) [49]. However, fabricating $SrBi_2Ta_2O_9$ thin films with *a*-oriented crystallinity and a *c*-axis-aligned in-plane orientation is much more challenging because of the large lattice mismatch between the *c*-axis of $SrBi_2Ta_2O_9$ and common $SrTiO_3$ single-crystal substrates [49]. Even though the P_r of partially *a*-oriented $SrBi_2Ta_2O_9$ thin film can be further improved to 35.3 μC·cm^{-2} [50], the leakage current issue has not been fully addressed, where the estimated conductivity of ~1.59×10^{-8} S·cm^{-1} at room temperature is not much smaller than that of *a*–*b* plane samples of textured $Sr_{1-x}Ca_xBi_2Ta_2O_9$ ceramics at 350 °C (6.89×10^{-8} S·cm^{-1} for x = 0 and 1.72×10^{-8} S·cm^{-1} for x = 0.4).

Apart from Ca doping, many other attempts to stoichiometrically or nonstoichiometrically substitute Sr, Bi, or Ta sites of $SrBi_2Ta_2O_9$ have also been explored. For example, substitution of the Sr site by rare-earth elements increases the remnant polarization while decreasing the Curie temperature [51], although Sm doping can improve the resistivity of $SrBi_2Ta_2O_9$ ceramics [20]. V-doped $SrBi_2Ta_2O_9$ ceramics with a texture degree of f ≈ 0.8 can achieve a higher dielectric constant and Curie temperature compared with those of pure $SrBi_2Ta_2O_9$, but the dielectric loss is unable to be effectively reduced (tanδ > 0.01) [52]. The synergistic improvement of the electrical performance in $SrBi_2Ta_2O_9$ is attributed not only to the microscopic strain induced by the different ionic radii of the doping element but also to certain electronic interactions between the doping element and the substituted element.

4 Conclusions

In summary, the improvement of in-plane ferroelectric polarization with a low in-plane leakage current of $SrBi_2Ta_2O_9$ ceramics is successfully achieved by texturing and Ca doping strategies. The in-plane ferroelectricity is fully released in the *a*–*b* plane sample with P_r = 15.83 μC·cm^{-2} in highly textured $SrBi_2Ta_2O_9$ ceramics (f = 0.985). Ca-doped $SrBi_2Ta_2O_9$ texture ceramics with a high degree of orientation (f ≥ 0.917) show an improved Curie temperature (T_C = 325–500 °C) and reduced in-plane leakage current density (J = 5.924×10^{-7} A·cm^{-2}@50 kV·cm^{-1}

for x = 0.4). The mechanism of Ca doping is clarified, where Ca substitution enhances P_s by increasing the polarization of the $[(Sr/Ca)Ta_2O_7]^{2-}$ perovskite unit and suppresses the in-plane leakage current by increasing the electronic band gap. Our methodology combining texture technology and a doping strategy provides guidance for designing high-performance $SrBi_2Ta_2O_9$ ferroelectric devices.

Acknowledgements

The authors thank Dr. Yongchun Zou and Mr. Pengcheng Nie for the TEM measurement. We acknowledge the characterization support from the Analysis and Testing Center of Harbin Institute of Technology.

Availability of data and materials

The data that support the findings of this study are available from the corresponding author upon reasonable request.

Competing interests

The authors have no competing interests to declare that are relevant to the content of this article.

Electronic Supplementary Material

Supplementary material is available in the online version of this article at https://doi.org/10.26599/JAC.2026.9221344.

References

[1] de Araujo CA, Cuchiaro JD, McMillan LD, *et al.* Fatigue-free ferroelectric capacitors with platinum electrodes. *Nature* 1995, **374**: 627–629.

[2] Scott JF, Paz de Araujo CA. Ferroelectric memories. *Science* 1989, **246**: 1400–1405.

[3] Mikolajick T, Slesazeck S, Mulaosmanovic H, *et al.* Next generation ferroelectric materials for semiconductor process integration and their applications. *J Appl Phys* 2021, **129**: 100901.

[4] Scott JF. Applications of modern ferroelectrics. *Science* 2007, **315**: 954–959.

[5] Shimakawa Y, Kubo Y, Nakagawa Y, *et al.* Crystal structures and ferroelectric properties of $SrBi_2Ta_2O_9$ and $Sr_{0.8}Bi_{2.2}Ta_2O_9$. *Appl Phys Lett* 1999, **74**: 1904–1906.

[6] Li JY, Rogan RC, Üstündag E, *et al.* Domain switching in polycrystalline ferroelectric ceramics. *Nat Mater* 2005, **4**: 776–781.

[7] Messing GL, Sabolsky EM, Kwon S, *et al.* Templated grain growth of textured piezoelectric ceramics. *Key Eng Mater* 2001, **206–213**: 1293–1296.

[8] Horn JA, Zhang SC, Selvaraj U, *et al.* Templated grain growth of textured bismuth titanate. *J Am Ceram Soc* 1999, **82**: 921–926.

[9] Seabaugh MM, Kerscht IH, Messing GL. Texture development by templated grain growth in liquid-phase-sintered α-alumina. *J Am Ceram Soc* 1997, **80**: 1181–1188.

[10] Duran C, Trolier-McKinstry S, Messing GL. Fabrication and electrical properties of textured $Sr_{0.53}Ba_{0.47}Nb_2O_6$ ceramics by templated grain growth. *J Am Ceram Soc* 2000, **83**: 2203–2213.

[11] Sabolsky EM, James AR, Kwon S, *et al.* Piezoelectric properties of <001> textured $Pb(Mg_{1/3}Nb_{2/3})O_3$–$PbTiO_3$ ceramics. *Appl Phys Lett* 2001, **78**: 2551–2553.

[12] Zhang XY, Wang Z, Li P, *et al.* Simultaneous achievement of large strain, low hysteresis, and high-temperature stability in textured BT-based piezoelectric ceramics. *J Adv Ceram* 2025, **14**: 9221025.

[13] Li FZ, Luo H, Cao L, *et al.* Sintering densification driven by orientation fluctuation in textured $BaTiO_3$ ceramics with abnormal comprehensive ferroelectric properties. *J Adv Ceram* 2025, **14**: 9221126.

[14] Tang XH, Li FZ, Tian JX, *et al.* Enhanced electrical properties in textured $Bi_4Ti_3O_{12}$ ceramics with negative strain. *Ceram Int* 2025, **51**: 15049–15054.

[15] Tian JX, Li FZ, Tang XH, *et al.* Sintering and enhanced ferroelectric properties of textured $Bi_5Ti_3FeO_{15}$ ceramics with high Curie temperature. *J Mater Chem C* 2025, **13**: 7358–7367.

[16] Tian JX, Cao L, Luo HJD, *et al.* Enhanced ferroelectric performance of textured $Bi_5Ti_3Fe_{1-x}Co_xO_{15}$ ceramics with room-temperature ferromagnetism. *Scripta Mater* 2025, **269**: 116919.

[17] Amorín H, Kholkin AL, Costa MEV. Texture development and dielectric properties of $SrBi_2Ta_2O_9$ ceramics processed by templated grain growth. *J Eur Ceram Soc* 2005, **25**: 2453–2456.

[18] Amorín H, Kholkin AL, Costa MEV. Templated grain growth of $SrBi_2Ta_2O_9$ ceramics: Mechanism of texture development. *Mater Res Bull* 2008, **43**: 1412–1419.

[19] Das RR, Bhattacharya P, Pérez W, *et al.* Influence of Ca on structural and ferroelectric properties of laser ablated $SrBi_2Ta_2O_9$ thin films. *Jpn J Appl Phys* 2003, **42**: 162–165.

[20] Kannan BR, Venkataraman BH. Dielectric and electrical conductivity characteristics of undoped and samarium doped ferroelectric $SrBi_2Ta_2O_9$ ceramics derived from molten salt synthesis route. *Ferroelectrics* 2016, **493**: 110–119.

[21] Noguchi Y, Shimizu H, Miyayama M, *et al.* Ferroelectric properties and structure distortion in A-site-modified $SrBi_2Ta_2O_9$. *Jpn J Appl Phys* 2001, **40**: 5812.

[22] Das RR, Pérez W, Katiyar RS, *et al.* Structural investigation of $(Sr_{1-x}Ca_x)Bi_2Ta_2O_9$ ceramics. *J Raman Spectrosc* 2002, **33**: 219–222.

[23] Das RR, Bhattacharya P, Pérez W, *et al.* Effect of Ca on structural and ferroelectric properties of $SrBi_2Ta_2O_9$ and $SrBi_2Nb_2O_9$ thin films. *Ceram Int* 2004, **30**: 1175–1179.

[24] Perez W, Das RR, Dobal PS, *et al.* Effect of cationic substitution on Raman spectra of $SrBi_2Ta_2O_9$ ceramics and thin films. *MRS Online Proc Libr* 2003, **784**: 329.

[25] Giannozzi P, Baroni S, Bonini N, *et al.* QUANTUM ESPRESSO: A modular and open-source software project for quantum simulations of materials. *J Phys—Condens Mat* 2009, **21**: 395502.

[26] Giannozzi P, Andreussi O, Brumme T, *et al.* Advanced capabilities for materials modelling with Quantum ESPRESSO. *J Phys—Condens Mat* 2017, **29**: 465901.

[27] Giannozzi P, Baseggio O, Bonfà P, *et al.* Quantum ESPRESSO toward the exascale. *J Chem Phys* 2020, **152**: 154105.

[28] Perdew JP, Burke K, Ernzerhof M. Generalized gradient approximation made simple. *Phys Rev Lett* 1996, **77**: 3865–3868.

[29] Perdew JP, Ruzsinszky A, Csonka GI, *et al.* Restoring the density-gradient expansion for exchange in solids and surfaces. *Phys Rev Lett* 2008, **100**: 136406.

[30] Vanderbilt D. Soft self-consistent pseudopotentials in a generalized eigenvalue formalism. *Phys Rev B* 1990, **41**: 7892(R)–7895(R).

[31] Miura K. Electronic properties of ferroelectric $SrBi_2Ta_2O_9$, $SrBi_2Nb_2O_9$, and $PbBi_2Nb_2O_9$ with optimized structures. *Appl Phys Lett* 2002, **80**: 2967–2969.

[32] Ramer NJ, Rappe AM. Virtual-crystal approximation that works: Locating a compositional phase boundary in $Pb(Zr_{1-x}Ti_x)O_3$. *Phys Rev B* 2000, **62**: R743–R746.

[33] Bellaiche L, Vanderbilt D. Virtual crystal approximation revisited: Application to dielectric and piezoelectric properties of perovskites. *Phys Rev B* 2000, **61**: 7877–7882.

[34] Henkelman G, Uberuaga BP, Jónsson H. A climbing image nudged elastic band method for finding saddle points and minimum energy paths. *J Chem Phys* 2000, **113**: 9901–9904.

[35] Sheppard D, Terrell R, Henkelman G. Optimization methods for finding minimum energy paths. *J Chem Phys* 2008, **128**: 134106.

[36] Chang YF, Wu J, Liu Z, *et al.* Grain-oriented ferroelectric ceramics with single-crystal-like piezoelectric properties and low texture temperature. *ACS Appl Mater Inter* 2020, **12**: 38415–38424.

[37] Thi MP, March G, Colomban P. Phase diagram and Raman imaging

of grain growth mechanisms in highly textured $Pb(Mg_{1/3}Nb_{2/3})O_3$–$PbTiO_3$ piezoelectric ceramics. *J Eur Ceram Soc* 2005, **25**: 3335–3346.

[38] Yang S, Li JL, Liu Y, *et al.* Textured ferroelectric ceramics with high electromechanical coupling factors over a broad temperature range. *Nat Commun* 2021, **12**: 1414.

[39] Amorín H, Costa MEV, Kholkin AL, *et al.* Electrical properties of $SrBi_2Ta_2O_9$ single crystals grown by self-flux solution. *J Eur Ceram Soc* 2004, **24**: 1535–1539.

[40] Subbarao EC. A family of ferroelectric bismuth compounds. *J Phys Chem Solids* 1962, **23**: 665–676.

[41] Amorín H, Shvartsman VV, Kholkin AL, *et al.* Ferroelectric and dielectric anisotropy in high-quality $SrBi_2Ta_2O_9$ single crystals. *Appl Phys Lett* 2004, **85**: 5667–5669.

[42] Shoji K, Aikawa M, Uehara Y, *et al.* Preparation and properties of $SrBi_2Ta_2O_9$ ceramics. *Jpn J Appl Phys* 1998, **37**: 5273.

[43] Swain S, Kumar P, Choudhary RB. Electrical and ferroelectric studies of the 2-layered $SrBi_2Ta_2O_9$ based ceramics. *Physica B* 2015, **477**: 56–63.

[44] Mun J, Huang FT, Pivak Y, *et al.* Probing ferroelectric domain structures and their switching dynamics in $SrBi_2Ta_2O_9$ by *in-situ* electric biasing in transmission electron microscopy. *Commun Mater* 2024, **5**: 145.

[45] Li FZ, Zhang HJ, Luo HJD, *et al.* Dual-channel dielectric tunability in highly textured $BaTi_{0.99}Fe_{0.01}O_{3-\delta}$ ceramics with micro-twin boundary. *Adv Electron Mater* 2023, **9**: 2201243.

[46] Shimakawa Y, Kubo Y, Nakagawa Y, *et al.* Crystal structure and ferroelectric properties of $ABi_2Ta_2O_9$ (A = Ca, Sr, and Ba). *Phys Rev B* 2000, **61**: 6559–6564.

[47] Li YX, Chen G, Zhang HJ, *et al.* Electronic structure and photocatalytic properties of $ABi_2Ta_2O_9$ (A = Ca, Sr, Ba). *J Solid State Chem* 2008, **181**: 2653–2659.

[48] Cai MQ, Yin Z, Zhang MS. Electronic structures and ferroelectric properties of $ABi_2Ta_2O_9$ (A = Ca, Sr, and Ba). *Solid State Commun* 2005, **133**: 663–666.

[49] Ahn Y, Son JY. Enhanced ferroelectric and piezoelectric properties of $SrBi_2Ta_2O_9$ thin films through crystalline orientation. *Solid State Sci* 2024, **153**: 107558.

[50] Lee E, Son JY. Domain wall current, ferroelectric, and piezoelectric properties of flexible $SrBi_2Ta_2O_9$ thin films affected by the distribution of *a*-oriented domains and *c*-oriented domains. *J Phys Chem Solids* 2024, **192**: 112074.

[51] Noguchi Y, Miyayama M, Oikawa K, *et al.* Defect engineering for control of polarization properties in $SrBi_2Ta_2O_9$. *Jpn J Appl Phys* 2002, **41**: 7062–7075.

[52] Wu CC, Yang CF. Effect of V_2O_5 B-site substitution on the microstructure, Raman spectrum, and dielectric properties of $SrBi_2Ta_2O_9$ ceramics. *Sci Rep* 2020, **10**: 19147.